STRAIN ENGINEERING

Role of scaffold network in controlling strain and functionalities of nanocomposite films

10.1126/sciadv.1600245

Aiping Chen,[1]* Jia-Mian Hu,[2] Ping Lu,[3] Tiannan Yang,[2] Wenrui Zhang,[4] Leigang Li,[4] Towfiq Ahmed,[5] Erik Enriquez,[1] Marcus Weigand,[1] Qing Su,[4] Haiyan Wang,[4] Jian-Xin Zhu,[5] Judith L. MacManus-Driscoll,[6] Long-Qing Chen,[2] Dmitry Yarotski,[1] Quanxi Jia[1]*

Strain is a novel approach to manipulating functionalities in correlated complex oxides. However, significant epitaxial strain can only be achieved in ultrathin layers. We show that, under direct lattice matching framework, large and uniform vertical strain up to 2% can be achieved to significantly modify the magnetic anisotropy, magnetism, and magnetotransport properties in heteroepitaxial nanoscaffold films, over a few hundred nanometers in thickness. Comprehensive designing principles of large vertical strain have been proposed. Phase-field simulations not only reveal the strain distribution but also suggest that the ultimate strain is related to the vertical interfacial area and interfacial dislocation density. By changing the nanoscaffold density and dimension, the strain and the magnetic properties can be tuned. The established correlation among the vertical interface—strain—properties in nanoscaffold films can consequently be used to tune other functionalities in a broad range of complex oxide films far beyond critical thickness.

INTRODUCTION

Epitaxial strain provides an alternative way to chemical composition for manipulating charge/orbital/spin order in correlated complex oxides. In epitaxial heterostructures and conventional layered structures, tremendous efforts have been devoted to tuning functional properties such as superconductivity (*1*), ferroelectricity (*2*, *3*), ferromagnetism (*4*), antiferromagnetism (*5*), and multiferroicity (*6*) by epitaxial strain. Strain-induced tilting, rotation, and elongation of oxygen octahedrons in ferromagnetic perovskite oxides could significantly influence the physical properties such as Curie temperature (T_C), magnetic anisotropy, and magnetotransport properties (*7*). Wang and Li (*8*) reported an enhancement of the magnetoresistance (MR) in 5- to 15-nm-thick $Pr_{0.67}Sr_{0.33}MO_3$ films using out-of-plane tensile strain. Adamo *et al.* demonstrated that T_C and electrical properties of $La_{0.7}Sr_{0.3}MnO_3$ (LSMO) thin films (22 nm) strongly depend on the biaxial strain. It was found that a large strain was needed to noticeably affect the electron transport (*9*). In addition, strain-induced perpendicular magnetic anisotropy in $La_{2/3}Ca_{1/3}MnO_3$ thin films has been achieved in relatively thin layers (*10*).

Although such epitaxial strain–modified physical properties are fascinating, the thickness over which effective strain can be maintained is limited. In a conventional strain engineering framework, epitaxial strain is only effective below the critical thickness, which is usually less than a few tens of nanometers. Tuning electron transport by epitaxial strain has only been achieved in ultrathin layers because of the relaxation of epitaxial strains in relatively thick films. It was reported that epitaxial strain–induced MR decreased with increasing film thickness and diminished above 20 nm (*11*). Hence, tuning the magnetic and electron transport properties by strain in thick films is challenging. In addition, conventional strain engineering is achieved by selecting substrates with different lattice parameters (*9*). Currently available commercial substrates are, however, very few, and most of them are expensive. Therefore, it is difficult to tune the strain continuously by conventional strain engineering.

Vertically aligned heteroepitaxial nanoscaffolding films have been proposed to generate strain in thick films (*12*, *13*). In general, these nanocomposite films have two phases with vertically matched interface. The amount of vertical lattice strain depends on a number of factors such as lattice constant mismatch, elastic constant mismatch, and thermal expansion coefficient mismatch (*12*, *14*). Vertically aligned nanocomposites have been quite intensively studied to understand microstructures (*15*–*18*), interface couplings (*19*–*23*), electronic/ionic conduction along vertical interfaces (*24*–*27*), and strains (*28*, *29*). Although epitaxial strain has been demonstrated to be a critical factor in controlling functional properties in conventional thin films, the deep knowledge about strain in vertical nanoscaffolding films is lacking. A few critical questions are open: (i) What are the underlying factors that control the vertical lattice strain, (ii) what is the strain distribution and how to control it, and (iii) how to establish a correlation between strain and functional properties without the influence of other factors such as microstructure. It has been demonstrated that both microstructure and vertical strain play critical roles in controlling functionalities in nanoscaffolding films (*30*). Previous reports have focused on tuning MR by microstructure control (*16*, *17*, *31*–*33*). Hence, using the vertical strain to manipulate functionalities such as magnetic anisotropy, magnetism, and electron transport in ferromagnetic perovskite thick films has not been achieved. Using this unique vertical strain to tune functional properties can be used in many different fields.

Here, we demonstrate that, by using the proposed strain design approach, large vertical lattice strain in the LSMO matrix can be designed by selecting two phases with a large lattice mismatch and a large elastic modulus mismatch. Phase-field simulations not only determine the strain distribution in nanocomposites but also reveal that the vertical interfacial area between the scaffold network and film matrix and the

---

[1] Center for Integrated Nanotechnologies, Los Alamos National Laboratory, Los Alamos, NM 87545, USA. [2] Department of Materials Science and Engineering, Pennsylvania State University, University Park, PA 16802, USA. [3] Sandia National Laboratories, Mail Stop 1411, Albuquerque, NM 87185, USA. [4] Department of Electrical and Computer Engineering, Texas A&M University, College Station, TX 77843, USA. [5] Theoretical Division, Los Alamos National Laboratory, Los Alamos, NM 87545, USA. [6] Department of Materials Science and Metallurgy, University of Cambridge, Cambridge CB3 OFS, UK.
*Corresponding author. Email: apchen@lanl.gov (A.C.); qxjia@lanl.gov (Q.X.J.)

interfacial dislocation density at the vertical heterointerface determine the ultimate strain in nanocomposites. By controlling the vertical interfacial area (for example, nanoscaffold density and dimension), we systemically tune the strain up to 2%. The tunable strain significantly modifies the magnetic properties of the LSMO matrix. We have established correlations among vertical interface—strain—properties in nanoscaffolding thick films. The principle discovered in this work reaches beyond the material systems studied and can be generalized to a variety of functional materials for strain and functionality tuning.

RESULTS

Strain design in vertically aligned nanocomposite films

Similar to the lateral epitaxial growth, we define the lattice matching along the vertical interface as either domain matching (*m* lattices of phase A match with *m* + 1 lattices of phase B, *m* is an integer) or direct lattice matching as shown in fig. S1. In the case of direct matching of strained lattices, where *m* lattices of phase A match with *km* lattices of phase B (*m* and *k* are positive integer numbers), the lattice strain is usually large. The calculated lattice mismatch with direct lattice matching ranges from 2.3 to 8.7% (see table S1), which assumes that one phase is completely strained to match another phase (*20*, *33*–*37*). The reported experimental strain ranges from 1.0 to 2.2%. The measured strain is consistently smaller than the calculated lattice mismatch in all reported systems. Table S2 summarizes the composite films with domain matching (*12*, *17*, *24*, *27*, *29*, *38*, *39*). The overall calculated misfit strain is small and less than 3.32%. For example, domain matching between LSMO and ZnO produces a vertical strain of 0.5% in LSMO (*31*). A serious issue is that the reported experimental values are not consistent with the calculated values. For epitaxial thin film growth, direct lattice matching is possible when a misfit strain is less than a threshold of ~7% (*40*). In the vertical nanoscaffolding thin films, it is meaningful to determine the misfit threshold for direct lattice matching. According to table S1, the maximum lattice mismatch that allows direct lattice matching for the epitaxial growth of vertical nanocomposites is at least ~9%. After selecting the epitaxial framework, lattice constants, elastic constants, and thermal expansion coefficient are important factors for designing systems with large strain (fig. S1). As we will demonstrate, the ultimate strain of a specific system in the synthesis stage is directly related to the vertical interfacial area and the interfacial dislocation density between these two phases, which can be tuned by volume fraction and growth condition (fig. S1). These three steps guide to design large strain in vertical nanoscaffolding films.

Microstructure characterizations of vertically aligned nanocomposite films

Both plan-view and cross-section transmission electron microscopy (TEM)/scanning transmission electron microscopy (STEM) have been conducted to understand the growth and the microstructure of LSMO:MgO films. Figure 1A shows a typical cross-section STEM image of the film with MgO nanoscaffold (22%, if not specifically mentioned, represents the volume fraction) in the LSMO matrix. The dark contrast represents the MgO phase, whereas the light contrast indicates the LSMO phase because the atomic Z number of Mg is much smaller than that of La. The phase separation is further confirmed by plan-view STEM (Fig. 1A, inset). It shows that MgO nanoscaffolds with a feature size of about 4 nm are randomly embedded in the LSMO matrix. The MgO nanoscaffolds penetrate through the whole film thickness (fig. S2). The high quality of the nanocomposite film is evidenced by the sharp diffraction dots (fig. S2). Figure 1B shows that both LSMO and MgO phases are vertically aligned on the STO substrate. It is interesting to note the formation of one to two unit cells of LSMO on top of the STO substrate before the growth of the MgO phase (Fig. 1C). The direct growth of LSMO (one to two unit cells) on STO is because the mismatch between LSMO and STO is only about 1%, whereas that between MgO and STO is larger than 7%. The formation of a layer that has a smaller lattice mismatch with the substrate is energetically favorable. In $BiFeO_3$:CoF_2O_4 nanocomposites, a few unit cells of BFO were formed on the SRO/STO surface before the growth of $CoFe_2O_4$ (*41*). Figure 1D illustrates typical vertical heterointerface between the LSMO and MgO phases. Although there is a large lattice mismatch of ~8.41% between LSMO and MgO, the heterointerface matches reasonably well along the thin film growth direction (fig. S2). These results indicate that high-quality nanoscaffolding films with epitaxial MgO nanoscaffolds in the LSMO matrix have been synthesized.

Robust strain tunability in vertically aligned nanocomposite films

Typical 2θ-ω scans of LSMO:MgO nanocomposite films show that both LSMO and MgO phases are (00*l*) oriented on the STO substrate,

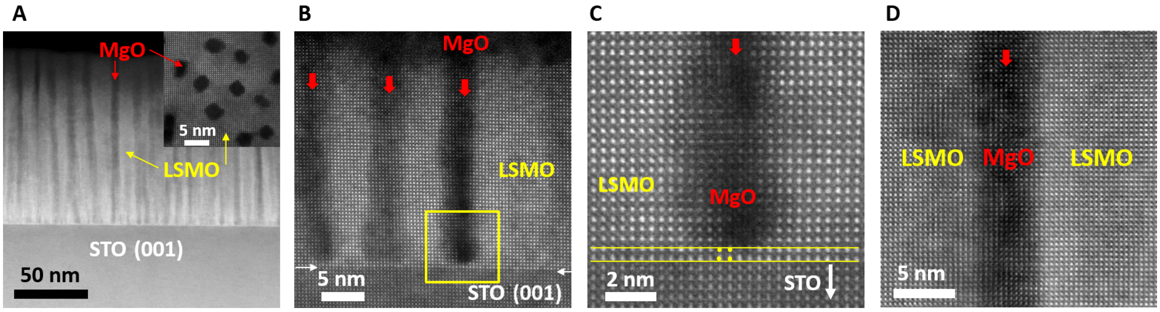

Fig. 1. Microstructure of nanoscaffolding films. (**A**) Cross-section STEM image showing the alternating growth of LSMO (white) and MgO vertical nanoscaffolds (dark) on STO (001) substrates. Inset: Plan-view STEM image of the LSMO:MgO films with 22% MgO phase, which shows the MgO nanoscaffolds, with a feature size of ~4 nm, in the LSMO matrix. (**B**) High-resolution STEM image showing the vertical MgO nanoscaffolds in LSMO phase. The red arrows point out MgO nanoscaffolds. (**C**) Zoomed-in yellow box area in (B) showing the film-substrate interface. One unit cell of LSMO transition layer is formed between nanocomposite film and substrate. (**D**) High-resolution STEM image showing the vertical interface between the MgO and LSMO phase.

without any detectable impurity phase (fig. S3). To study the strain tunability in the LSMO phase by the density of MgO nanoscaffolds, nanocomposite films with different MgO content *x* were grown on the STO substrate (fig. S3). Reciprocal space mapping (RSM) has been conducted to determine strain states. Figure 2 (A and B) shows the RSM for LSMO:MgO (40%) nanocomposite films, around the STO (002) and (103) peaks, respectively. "X_1" and "Δ" represent the positions of single-phase LSMO and MgO films, respectively (fig. S4). "X_2" represents the position of the LSMO phase after incorporating MgO nanoscaffolds. The inclusion of MgO nanoscaffolds downshifts the LSMO peaks in the Q_z direction and moves the peak from the X_1 position to the X_2 position (Fig. 2, A and B), indicating an elongation of the LSMO out-of-plane lattice parameter. In contrast, MgO peak upshifts in the Q_z direction, indicating a compression of MgO out-of-plane lattice parameter (fig. S4). This is a direct evidence of the vertical lattice coupling.

The strain of the LSMO phase in the nanocomposites is summarized in Fig. 2C. The out-of-plane lattice parameter of the LSMO phase has been changed from 3.852 Å (compression) in the single-phase LSMO film to 3.896 Å (tension) in the LSMO:MgO (15%) (fig. S4). By increasing the nanoscaffold density further (40% MgO volume), the out-of-plane parameter of the LSMO matrix increases to 3.938 Å (table S3). As shown in Fig. 2C, the strain of the LSMO phase gradually increases and tends to reach a plateau by increasing the MgO nanoscaffold density. Remarkably, the tensile strain in the LSMO phase is as large as ~2% in the nanocomposite films (*x* = 40%). The increase of nanoscaffold density would increase the vertical heterointerface area and produce larger strain in thick nanocomposite films. It should be noted that such a large strain in relatively thick films is not feasible for conventional strain engineering because of the formation of misfit dislocations above the critical thickness. To demonstrate that the nanoscaffold phase plays a critical role in controlling the strain state of the nanocomposite films, the strain in the LSMO:ZnO films has also been plotted in Fig. 2C. It can be seen that the strain in the LSMO matrix slightly increases with incorporating ZnO nanoscaffolds, but the magnitude is much smaller.

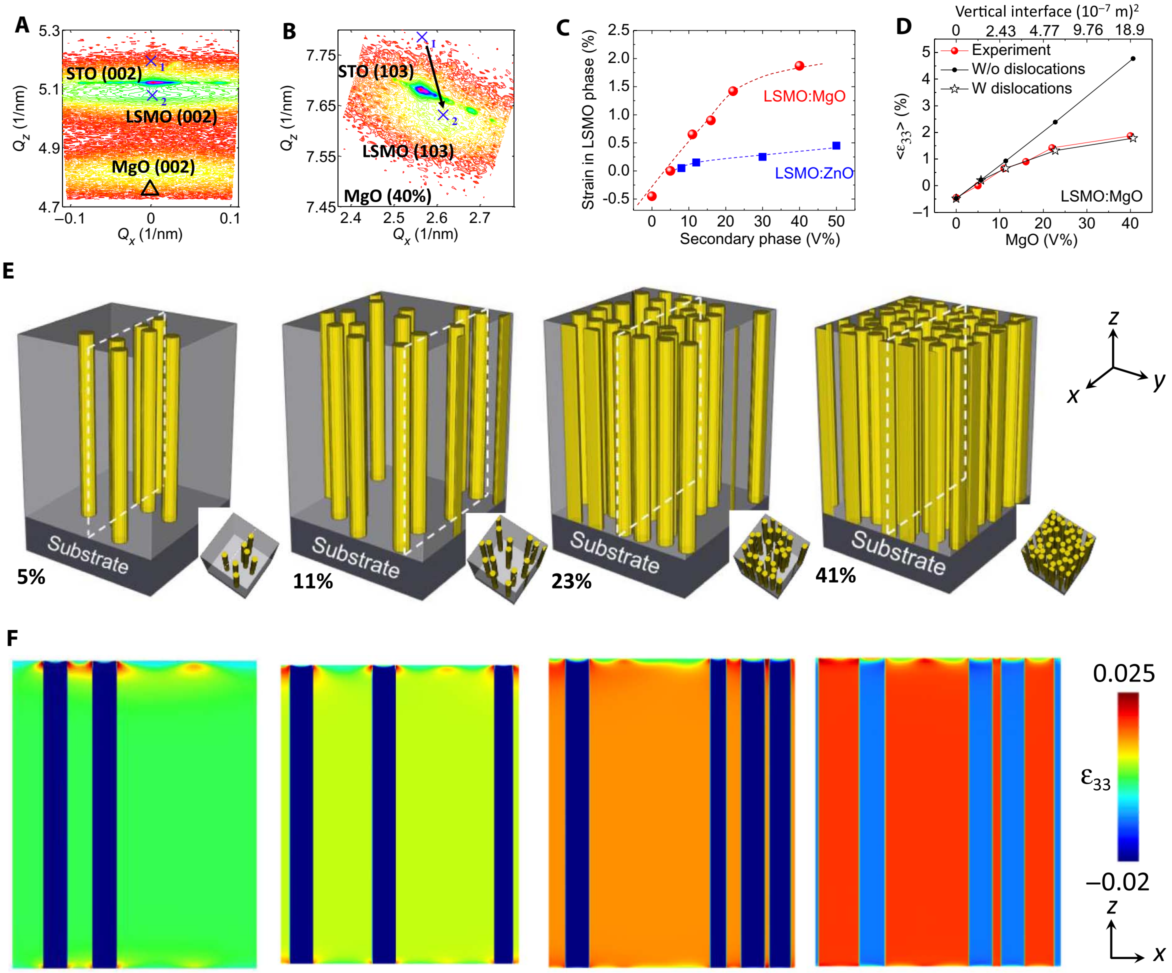

Fig. 2. Nanoscaffold density–dependent strain and its distribution simulated by the phase-field method. (**A** and **B**) RSM (002) (A) and RSM (103) (B) of 450-nm nanocomposite films with 40% MgO. (**C**) Relationship between the strain state in the LSMO phase and the scaffold phase volume ratio (red represents MgO, and blue curve represents ZnO). (**D**) Simulated out-of-plane strain in LSMO:MgO by phase-field model with and without considering misfit dislocations. Top *x* axis represents the circumference obtained from simulations at different MgO volumes. (**E**) Schematic drawing of MgO nanoscaffold in the LSMO matrix with different MgO volume ratios (from left to right: ~5, ~11, ~23, and ~41%, respectively). (**F**) Calculated strain distribution in the LSMO matrix and MgO nanoscaffolds in the plane marked as white dash lines in (E) for different MgO compositions (from left to right: ~5, ~11, ~23, and ~41%, respectively). The film thickness of this simulated film is 250 nm.

The vertical strain in LSMO:MgO nanocomposite films is far larger than that in LSMO:ZnO with the same volume fraction of the nanoscaffold. The lattice mismatch between LSMO and ZnO through domain matching is only 0.46%, whereas that between the LSMO and MgO system is 8.41%. The elastic modulus of MgO is also larger than that of ZnO (table S4). Both larger lattice mismatch and elastic modulus mismatch are responsible for the larger strain state in the LSMO:MgO. It indicates that direct lattice matching with both a large lattice mismatch and elastic modulus mismatch gives rise to vertically aligned epitaxial nanoscaffolds with large vertical strain.

Strain state and its spatial distribution by phase-field simulations

We have demonstrated that the strain in the matrix can be tuned by changing the nanoscaffold network. To study the spatial distribution of strain in the matrix, we performed three-dimensional (3D) phase-field simulations (see Materials and Methods). Figure 2E shows the microstructure of computationally constructed nanoscaffolding films with MgO nanoscaffolds randomly embedded in the LSMO matrix (MgO fraction ranging from ~5 to ~41%). It is consistent with experimental observation (Fig. 1A). Figure 2F shows the simulated distribution of the out-of-plane strain in the nanocomposite films with a thickness of 250 nm. The strain distribution in nanocomposite films is uniform. Appreciable strain nonuniformity only occurs at the substrate-film and film-air interfaces. The uniformity of strain distribution is strongly related with film thickness. Completely opposite to conventional single-phase planar films, the thicker the film is, the better the strain uniformity is (fig. S5). The increased overall strain with increasing the nanoscaffold density is almost independent of film thickness. Figure 2D shows that, if misfit dislocations are not considered in the model, the overall strain increases linearly with the increasing MgO volume fraction and the increasing vertical heterointerface area. Rather, the effective vertical strain follows a linear relationship when the MgO volume is less than 10% but deviates from the linear relationship at the larger MgO volume fractions because of the formation of misfit dislocations. The calculated out-of-plane strains agree with experimental results when dislocations are properly accounted for. The phase-field simulation results suggest that the strain status is directly related with the vertical interfacial area and the misfit dislocation at the heterointerface between MgO nanoscaffolds and the LSMO matrix. That is, the ultimate strain is controlled by the vertical coherent interfacial area.

Tuning functionality by varying nanoscaffold density

The strain in vertically aligned nanocomposite films can be tuned by changing the nanoscaffold density. This consequently manipulates the physical properties of the active phase such as LSMO, including the magnetic anisotropy and magnetotransport behaviors. The inset of Fig. 3A shows the magnetic hysteresis (*M-H*) loop of LSMO:MgO nanocomposite film with 5% MgO. This film exhibits an in-plane easy axis. Perpendicular magnetic anisotropy was observed in LSMO:MgO (15%) nanocomposite films (Fig. 3A). With increasing of the MgO nanoscaffold density, the easy axis of films switches from in-plane to out-of-plane. Strain has been considered to be a key factor for magnetic anisotropy in single-phase films (*42*, *43*). The switching of magnetic anisotropy in nanocomposite films is correlated with the strain in the LSMO matrix. To exclude the microstructure effect on the magnetic anisotropy, the

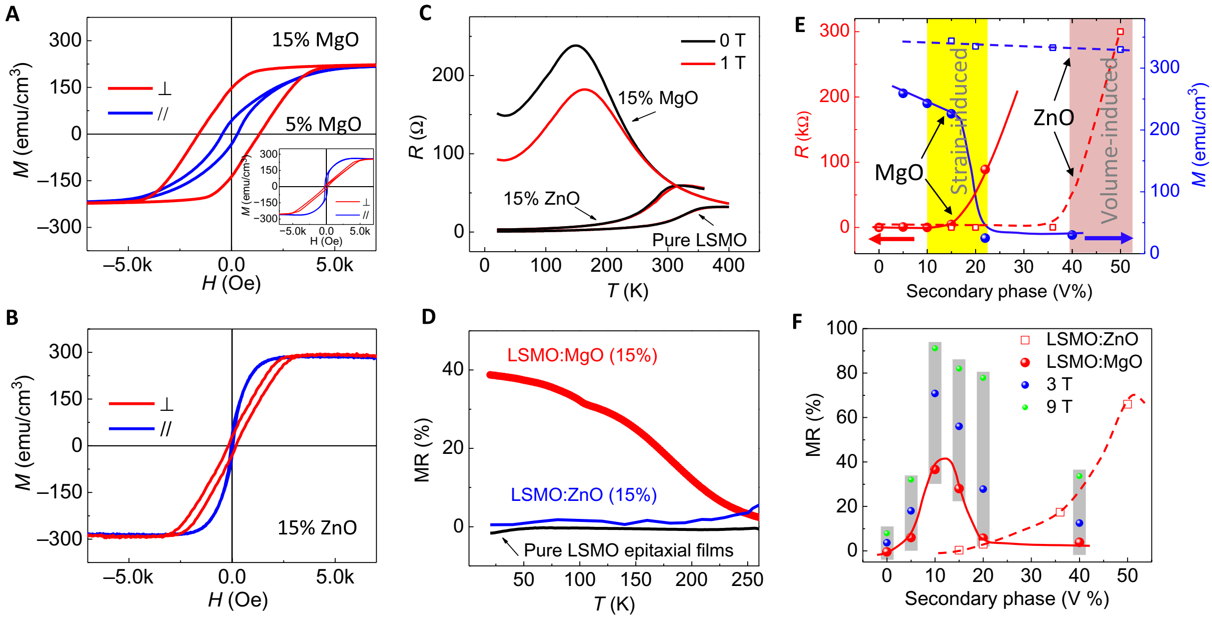

Fig. 3. Nanoscaffold density–dependent magnetic properties. (**A**) *M-H* loops of LSMO:MgO (15%) nanocomposite films. The inset is *M-H* loops of LSMO:MgO (5%) films. (**B**) *M-H* loops of LSMO:ZnO (15%) nanocomposite films. (**C**) *R-T* curves at 0 and 1 T for LSMO:ZnO (15%), LSMO:MgO (15%), and a reference LSMO film. (**D**) MR-*T* (1 T) curves for LSMO:ZnO, LSMO:MgO, and a reference LSMO film. (**E**) Scaffold phase volume ratio–dependent resistance at 100 K (red) and saturated magnetization (blue) at 20 K for LSMO:ZnO (15%) and LSMO:MgO (15%) films. The magnetizations have been normalized to the volume of LSMO. "Strain-induced" means that magnetization and resistance change are induced by the strain effect. "Volume-induced" means that resistance change is dominated by the volume effect. (**F**) Scaffold phase volume fraction–dependent MR (1 T, red) at 130 K for the LSMO:ZnO and LSMO:MgO films. The blue and green data points are MR measured under 3 and 9 T, respectively, for the LSMO:MgO films. The gray square highlights the MR measured at the same temperature but different magnetic fields.

M-H of LSMO:ZnO (15%) nanocomposite films exhibiting an in-plane easy axis is shown in Fig. 3B. These experimental results show that strain dominates the magnetic anisotropy of nanocomposite films. Figure 3C shows the temperature-dependent resistance in pure LSMO, LSMO:ZnO (15%), and LSMO:MgO (15%) thin films. These films exhibit different metal-insulator transition temperatures (T_{MI}). The T_{MI} of pure epitaxial LSMO film is ~350 K, which is close to the bulk value. A lower T_{MI} (315 K) is expected from LSMO:ZnO (15%) nanocomposite films. However, the T_{MI} for LSMO:MgO (15%) is only 150 K, which is significantly lower than that of LSMO:ZnO. The large vertical strain could be responsible for the large drop of T_{MI} in the LSMO:MgO system (*9*).

The MR at 1 T is plotted in Fig. 3D. It can be seen that, across a very broad temperature range, the LSMO:MgO films exhibit significantly enhanced MR compared to LSMO:ZnO with the same volume fraction of the scaffold phase. For example, the MR (1 T) of LSMO:MgO (15%) at 20 K is ~40%, whereas that of LSMO:ZnO (15%) is only ~3%. The resistance and magnetization versus scaffold phase volume are plotted in Fig. 3E (red and blue, respectively). The significant increase in resistance in the LSMO:ZnO system occurs when ZnO volume approaches 50%. We defined the 50% as a volume-induced resistance transition threshold. In LSMO:MgO, however, the marked increase of resistance occurs at 15 to 20% of MgO, which is far below the volume percolation threshold in the LSMO:ZnO system. Hence, the strain could be the dominating factor that leads to a conductivity threshold of scaffold phase being as low as ~20%. We defined this 20% as a strain-induced resistance transition threshold. Another striking difference between LSMO:MgO and LSMO:ZnO is the volume-dependent magnetization, plotted in blue in Fig. 3E. The magnetization in LSMO:ZnO reduces slightly with increasing the ZnO volume. However, the magnetization in the LSMO:MgO system experiences a significant drop across ~20% of the scaffold phase. The sharp drop of magnetization over 10 times [from ~259 to ~25 electromagnetic units (emu)/cm^3] is another evidence that strain plays a critical role in determining the physical properties of LSMO:MgO (Fig. 3E, solid blue curve). Figure 3F shows the volume (scaffold phase)–dependent MR in both films. Largely enhanced MR in LSMO:MgO is located close to the strain-induced threshold (10 to 20% MgO). The MR maximum in LSMO:ZnO is located at the volume percolation threshold (50% ZnO). These results have demonstrated that the magnetic and magnetotransport properties in LSMO:MgO nanocomposite films are dominated by the vertical lattice strain.

Tuning functionalities by varying scaffold dimension

Another way of tuning the vertical strain is varying the feature size of nanoscaffolds as it changes the area of vertical heterointerface. To tune the size, LSMO:MgO (22%) nanocomposite films have been grown at different temperatures. Figure 4A shows the symmetrical RSM scan close to STO (002). The upshift of the LSMO (002) peak and the downshift of the MgO (002) peak in the Q_z axis with increasing the growth temperature suggest a decrease of the LSMO out-of-plane lattice parameter and an increase of the MgO out-of-plane lattice parameter. It reveals the weakening of the strain coupling along the heterointerface with increasing the growth temperature (fig. S6). The higher the growth temperature is, the smaller the strain is. Higher growth temperature results in larger thermal diffusion coefficient and larger nanoscaffold size. As shown in Fig. 4B, the dimension of MgO nanoscaffolds grown at 900°C (average, 16.8 nm) is larger than that grown at 835°C (average, 11.4 nm). The temperature-dependent nanoscaffold dimension is shown in Fig. 4C. The diffusion-controlled growth mechanism is evidenced by the fitting to an Arrhenius equation

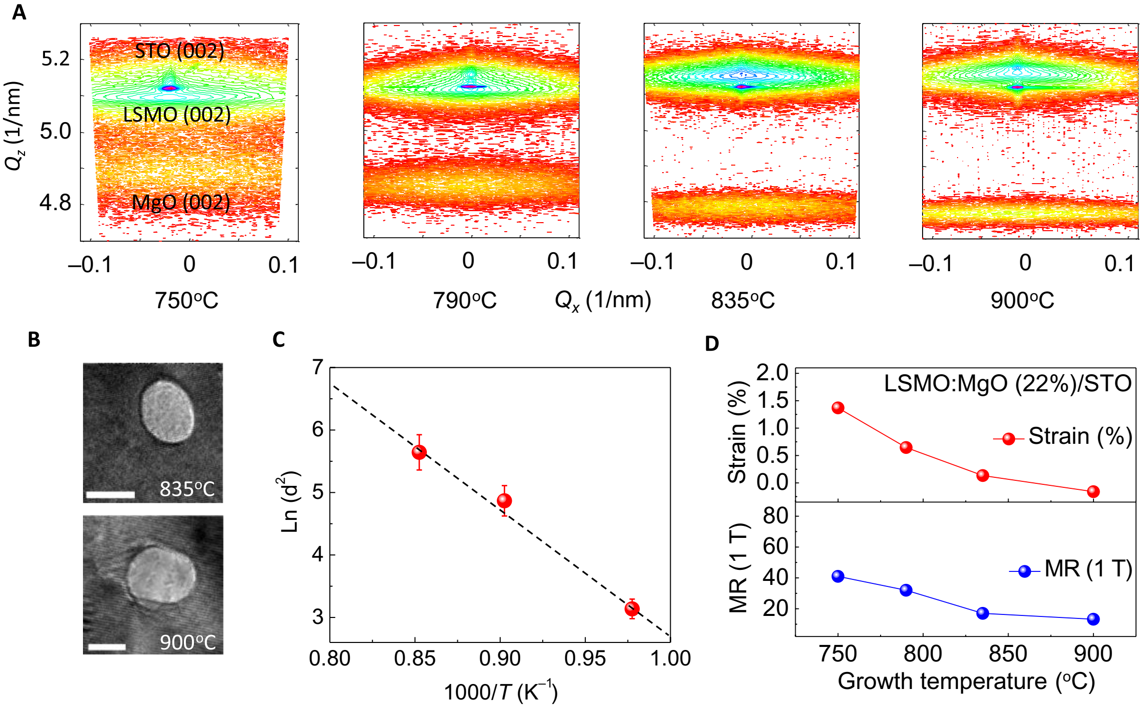

Fig. 4. Nanoscaffold dimension–dependent strain and properties. (**A**) RSM (002) of 600-nm LSMO:MgO (22%) nanocomposite films grown at different temperatures (from left to right: 750°, 790°, 835°, and 900°C, respectively). (**B**) Plan-view TEM images of films grown at 835° and 900°C, respectively. Scale bars, 10 nm. (**C**) Temperature-dependent nanoscaffold feature size. (**D**) Growth temperature–dependent strain and MR (20 K).

(*44*). Figure 4D shows that both strain and MR decrease with increasing growth temperature. In the intermediate strain region (strain less than 1.5%), relatively larger strain results in higher MR.

DISCUSSION

The magnetic anisotropy in nanocomposite films is analyzed by vertical strain. Because the magnetocrystalline anisotropy energy is equivalent along the [001], [010], and [100] directions, the magnetic anisotropy is determined by magnetoelastic anisotropy energy and demagnetization energy. The demagnetization energy $2\pi M^2$ is determined to be 3.93×10^5 ergs/cm^3, considering that the saturated magnetization M is 226 emu/cm^3 (15% MgO). The magnetoelastic anisotropy energy along the film growth direction is given by $K_{me} = 3\lambda_{[001]}Y_{[001]}\varepsilon_{oop}/2$, where $\lambda_{[001]}$ is the magnetostriction coefficient along the [001] direction. $Y_{[001]}$ is given by $Y = (C_{11} - C_{12})(C_{11} + 2C_{12})/(C_{11} + C_{12})$ (*45*), where the elastic constants for LSMO are $C_{11} = 2.27 \times 10^{12}$ dynes/cm^2, $C_{12} = 1.58 \times 10^{12}$ dynes/cm^2 (*46*), and $\lambda_{[001]}$ ~100 ppm (*47*). ε_{oop} is the strain along the out-of-plane direction. The lattice parameters, strain states, and strain anisotropy energy of the LSMO matrix are summarized in table S3. With a small amount of MgO (for example, MgO <5%) in the matrix, both shape anisotropy and strain anisotropy (c/a <1) prefer the in-plane easy axis. With increasing MgO volume (>5%), perpendicular magnetic anisotropy is observed because the large out-of-plane strain anisotropy energy induced by the scaffolds dominates (table S3). In addition to the strain-controlled magnetic anisotropy, the higher strain is also responsible for the markedly reduced magnetization in LSMO:MgO. The large strain results in lattice distortion, oxygen vacancies, and octahedral tilting/rotation, which can significantly modify the ferromagnetism in LSMO (*7*, *48*). Our density functional theory (DFT) calculation suggests that strain-induced oxygen octahedral distortion markedly reduces the magnetization (fig. S7) (*7*, *9*, *49*).

Moshnyaga *et al.* reported a phase transition–induced large colossal MR in $La_{0.7}Ca_{0.3}MnO_3$:MgO films. However, the MgO boundary played a significant role in the magnetotransport, because MgO phases were concentrated exclusively within the phase boundaries of the $La_{0.7}Ca_{0.3}MnO_3$ phases (*33*). Previous results have demonstrated that the microstructure itself plays an important role in controlling the magnetotransport properties (*16*, *17*). To establish the correlation between strain and functional properties, we have eliminated the microstructure effect in our study by comparing the properties in the LSMO:MgO and LSMO:ZnO films with the same volume of the scaffold phase (10 to 20%). It is well below the volume percolation threshold. When the nanoscaffold density is low (10 to 20%), carriers tend to conduct in the LSMO phase because the LSMO is well connected as a matrix (Fig. 1A, inset). Therefore, the MgO pillars do not serve as tunneling barrier when the secondary phase content is well below the percolation threshold. In addition, the effect of dimension confinement on physical properties is very limited when the secondary phase volume is low. For example, the T_C and magnetization of LSMO:ZnO nanocomposites with 10% ZnO in volume are almost the same as those of the pure LSMO films. Therefore, the enhanced MR in LSMO:MgO, compared to LSMO:ZnO, is dominated by the vertical strain effect.

The strain in nanocomposite films is controlled by the contact area of the vertical heterointerface. The nanoscaffold MgO vertical surface area S is linearly proportional to its volume V if the dimension of the scaffolds size is constant (fig. S8). Experimentally, the strain increases linearly with the MgO volume (vertical interfacial area between MgO and LSMO) when the MgO volume is less than 10% (Fig. 2D). At higher MgO volumes, the interfacial dislocation density increases. This is a dominating factor for the deviation of strain from the linear relationship. In addition, randomly distributed nanoscaffolds tend to contact each other, which slows down the increased rate of the total vertical interfacial area (fig. S9). This can be another factor for the strain deviation. In the case of increasing the nanoscaffold dimension with a fixed volume fraction, the vertical surface area is inversely proportional to the nanoscaffold dimension (fig. S10). Thus, the strain and the MR gradually increase with decreasing nanoscaffold feature size (Fig. 4D).

In conclusion, we demonstrated that, via the framework—design—synthesis approach, large and uniform vertical strain can be achieved in thick nanocomposites. Phase-field simulations have predicted strain distribution in thick nanoscaffolding films and determined that the vertical interfacial area and interfacial dislocation density between the scaffold network and film matrix control the ultimate strain status. Experimental results confirm theoretical conclusions and prove that the vertical strain plays a critical role in manipulating magnetism, magnetic anisotropy, and low-field magnetotransport in thick nanoscaffolding films. Therefore, this work provides guidance to design large strain in nanoscaffolding films and use the large vertical strain to tune functional properties beyond magnetism and magnetotransport.

MATERIALS AND METHODS

Film growth

The vertically aligned LSMO:MgO nanocomposite films (250 to 600 nm) were heteroepitaxially grown on STO (001) substrates by pulsed laser deposition (Lambda Physik, 248 nm, 2 J/cm^2). An image beam method was used to obtain stabilized and uniform laser energy density on the target (*50*). The composite targets were synthesized by the conventional ceramic sintering process. The oxygen pressure is kept at 100 mtorr, and substrate temperature ranges from 750° to 900°C during deposition of films. The growth rate was ~0.25 Å/pulse. All samples were post-annealed at 600°C for 60 min under 600-torr oxygen to minimize the oxygen vacancies. After annealing, samples were cooled down to room temperature at 5°C/min.

Characterization

The structures were examined by high-resolution x-ray diffraction (XRD) (PANalytical's MRD) using Cu-K$_\alpha$ radiation (λ = 1.5406 Å). The microstructures were characterized by STEM/TEM (FEI Tecnai G^2 F20 and F30). An FEI Titan G^2 800-200 STEM (operated at 200 kV) with a probe Cs corrector and ChemiSTEM technology (X-FEG and SuperX EDS with four windowless silicon drift detectors) was used to record high-resolution STEM images. STEM high-angle annular dark-field images were recorded with an annular detector with a collection range of 0.6 to 1.6 mGy. The magnetotransport properties were investigated by Physical Properties Measurement System (PPMS, Quantum Design). During the magnetotransport measurements, the magnetic field up to 9 T was applied perpendicular to the film plane, and the current was applied in the film plan along the [100] direction. The resistance of nanocomposite films was measured during the warm-up process from 20 to 350 K at a heating rate of 2 K/min. Both out-of-plane and in-plane M-H loops were recorded by the vibrating sample magnetometer option in the PPMS at 10 K. Samples have been thermally demagnetized before measurements.

3D phase-field simulation of strain distribution

An in-house microstructure-property modeling package based on phase-field method (*51*), namely, μ-Pro, is used to calculate the effective out-of-plane strain (Fig. 2D) and the strain distribution (Fig. 2F). 3D discretized grids of $200\Delta x \times 200\Delta y \times 500\Delta z$ ($\Delta x \times \Delta y \times \Delta z$ = 1 nm × 1 nm × 1 nm) are constructed to describe four different phases including the substrate (the bottom 200 layers of grids), LSMO-MgO nanoscaffolding film (the middle 250 layers of grids, corresponding to a nominal film thickness of 250 nm), and the air (the top 50 layers of grids). The air phase with zero elastic stiffness constant is introduced to establish the stress-free boundary condition on the film surface. The strain distribution in the system is obtained by solving the mechanical equilibrium equation $\nabla \cdot [c(\varepsilon - \varepsilon^0)] = 0$, where c is the local elastic stiffness tensor; the total strain tensor ε is the sum of a homogeneous strain tensor ε^{hom} ($=a_{\text{STO}} - a_{\text{LSMO}}/a_{\text{LSMO}}$ for diagonal components and 0 for off-diagonal components), describing the substrate-imposed macroscopic deformation of the LSMO matrix, and a heterogeneous strain ε^{het} whose volume average is zero (*52*). ε^{het} is obtained on the basis of $\varepsilon^{\text{het}} = 0.5[(\nabla \cdot u)^T + (\nabla \cdot u)]$, with u representing the displacement tensor; ε^0 is the mismatch strain between the constituting solid phases and the reference phase (that is, the LSMO matrix, in which $\varepsilon^0 = 0$). Four field variables η_i (i = 1, 2, 3, 4) are introduced to describe the phases, for example, $\eta_1 = 1$ in the substrate phase, whereas $\eta_1 = 0$ in the other phases. In this case, the spatially variant elastic/strain/displacement tensors can be described using these field variables. For example, the elastic stiffness tensor can be written as $c = \sum_i c_i \eta_i$, where the subscript i (=1, 2, 3, 4) indicates a given phase. The mechanical equilibrium equation is solved using a Fourier spectral iterative perturbation method (*53*). Given the large lattice mismatch between the constituting phases, the influence of interfacial dislocations must be taken into account to properly predict the average out-of-plane strain as a function of the MgO pillar phase fraction (f_{MgO}); otherwise, the calculated strain would increase linearly with increasing f_{MgO} because of the linearly increased area of the LSMO-MgO interface, as shown in Fig. 2D. The elastic stiffness tensors of the MgO and STO are listed in table S4 (*46*, *54*–*56*).

We assume that the misfit dislocations form at the horizontal MgO-STO interface and the vertical LSMO-MgO interface because of their much larger lattice mismatch than that of the LSMO-STO interface. The ε^0 in the STO substrate is calculated as $\varepsilon^0 = (a_{\text{STO}} - a_{\text{LSMO}})/a_{\text{LSMO}} \approx 0.904\%$. The in-plane diagonal components of the residual (that is, after relaxation through forming dislocations) ε^0 in MgO pillars ($\varepsilon^0_{\text{IP}} = \varepsilon^0_{11} = \varepsilon^0_{22}$) are expressed as

$$\varepsilon^0_{\text{IP}} = \frac{-\varepsilon'_{\text{IP}} a_{\text{MgO}} + a_{\text{STO}} - a_{\text{LSMO}}}{a_{\text{LSMO}}}$$
$$\varepsilon'_{\text{IP}} = \varepsilon'_{f_{\text{MgO}}\to 0\%}\left(1 - f_{\text{MgO}}\right) + \varepsilon'_{f_{\text{MgO}}=100\%} f_{\text{MgO}} \tag{1}$$

where $\varepsilon'_{f_{\text{MgO}}\to 0\%}$ denotes the in-plane mismatch strain between the MgO phase and the STO substrate when there is an infinitesimally small amount of MgO pillars (for example, hypothetically, one single MgO pillar with small radius) in the LSMO film matrix. In this case, there is no space for the formation of dislocation at the STO-MgO interface, and hence, the substrate-induced strain [$\varepsilon_{\text{app}} = (a_{\text{STO}} - a_{\text{MgO}})/a_{\text{MgO}}$] can be fully imparted on the MgO pillar, that is, $\varepsilon'_{f_{\text{MgO}}\to 0\%} = \varepsilon_{\text{app}}$. As another extreme, $\varepsilon'_{f_{\text{MgO}}=100\%}$ denotes the mismatch between a continuous MgO film and the STO substrate. According to the formula by Qiu *et al.* (*57*), it can be written as

$$\varepsilon'_{f_{\text{MgO}}=100\%} = 1 - \frac{1 - \varepsilon_{\text{app}}}{1 - \varepsilon_{\text{app}}\left(1 - \frac{h_c}{h}\right)} \tag{2}$$

where h is the film thickness (≈250 nm) and h_c is the critical thickness beyond which the interfacial dislocation would appear. At h_c, the area elastic energy density cost of holding a nominal mismatch strain (in this case, about −7.24%) in the film, f_{elast}, equals the area energy density cost of forming an interfacial dislocation, f_{disl} (*58*). With this in mind, our derivation (see S1) suggest that (*59*), for an edge dislocation that is commonly observed a the film-substrate interface (*60*), h_c can be obtained by solving

$$\frac{h_c}{\ln\left(\frac{h_c}{b}\right)} = \frac{b}{8\pi(1+\nu)\varepsilon_{\text{app}}} \tag{3}$$

where $\nu = c_{12}/(c_{11} + c_{12})$ is the Poisson's ratio of the MgO and b is the magnitude of Burger's vector [$b \approx 2.977$ Å for an a/2<110> type edge dislocation in MgO (*59*)]. For the present ε_{app} of about −7.24%, solving Eq. 3 yields an h_c of about 1.2 Å. This further leads to $\varepsilon^0_{f_{\text{MgO}}=100\%}$ of about −0.0032%, suggesting an almost complete strain relaxation. Building on these, the residual in-plane mismatch strain in MgO (see Eq. 1) at a given f_{MgO} is calculated as a linear combination of $\varepsilon^0_{f_{\text{MgO}}\to 0\%}$ and $\varepsilon^0_{f_{\text{MgO}}=100\%}$ (see the second row in Eq. 1), followed by a conversion from the MgO reference to LSMO reference (see the first row in Eq. 1).

The out-of-plane diagonal component of the residual ε^0 in MgO pillars ($\varepsilon^0_{\text{OOP}} = \varepsilon^0_{33}$) is determined by the nominal mismatch between the vertical LSMO-MgO interface (denoted as ε_{app} as well) and the possible dislocations therein. $\varepsilon^0_{\text{OOP}}$ plays a dominant contribution to the calculated effective out-of-plane strain shown in Fig. 2D. By analogy to conventional horizontal film growth, we assume that there is a critical radius (R_c) for the MgO pillars beyond which the dislocations form at the vertical interface to relax the ε_{app}. The magnitude of R_c should not only decrease with increasing ε_{app} similarly to the case of h_c (cf. Eq. 3) but also decrease with increasing volume fraction of the MgO pillars (f_{MgO}). The latter is the major difference from conventional horizontal film growth. Bearing these in mind, we develop an analytical model to estimate R_c through the following equation (see details of derivation in the Supplementary Materials)

$$\frac{R_c}{\ln\left(\frac{2R_c}{b}\right)} = \frac{Gbk}{\left(1 - f_{\text{MgO}}\right)\sqrt{f_{\text{MgO}}}(1-\nu)\pi Y \varepsilon_{\text{app}}} \tag{4}$$

where $G = Y/[2(1 + \nu)]$ is the shear modulus of the MgO, Y is the Young's modulus, and k is a unitless prefactor ($k > 0$) that relates the volume fraction of the MgO pillars (f_{MgO}) to the radius of the dislocation loop surrounding the MgO pillars (see discussion in S1). Note that this k (=0.38 for the simulation results in Fig. 2D) is the only fitting parameter in our model. With known R_c, ε^0_{OOP} can then be calculated analogously to Eq. 2, where h_c should be replaced with R_c in the formula.

SUPPLEMENTARY MATERIALS

Supplementary material for this article is available at http://advances.sciencemag.org/cgi/content/full/2/6/e1600245/DC1
table S1. Vertical lattice strain reported in different systems with direct lattice matching.
table S2. Vertical lattice strain reported in different systems with domain matching.
table S3. The lattice parameters of LSMO:MgO nanoscaffolding films.
table S4. The elastic stiffness tensor of the materials used in our work.
fig. S1. Strain design flow in vertical nanocomposites.
fig. S2. Microstructure of LSMO:MgO nanoscaffolding films.
fig. S3. XRD of nanocomposites with different nanoscaffold density.
fig. S4. Strain state evaluated by RSM.
fig. S5. Thickness-dependent strain distribution in nanoscaffolding films.
fig. S6. XRD of nanocomposites with different nanoscaffold size.
fig. S7. Magnetic moments versus O-Mn-O angle by DFT calculation.
fig. S8. The relationship between MgO cylinder surface and MgO volume.
fig. S9. The simulated of nanoscaffolds in a matrix.
fig. S10. The relationship between MgO cylinder surface and its radius.
fig. S11. Critical radius and the residual vertical mismatch strain versus MgO volume.
S1. Deriving the analytical expressions of critical thickness (h_c) and radius (R_c) in vertical nanocomposite thin films

REFERENCES AND NOTES

1. I. Bozovic, G. Logvenov, I. Belca, B. Narimbetov, I. Sveklo, Epitaxial strain and superconductivity in $La_{2-x}Sr_xCuO_4$ thin films. *Phys. Rev. Lett.* **89**, 107001 (2002).
2. J. H. Haeni, P. Irvin, W. Chang, R. Uecker, P. Reiche, Y. L. Li, S. Choudhury, W. Tian, M. E. Hawley, B. Craigo, A. K. Tagantsev, X. Q. Pan, S. K. Streiffer, L.-Q. Chen, S. W. Kirchoefer, J. Levy, D. G. Schlom, Room-temperature ferroelectricity in strained $SrTiO_3$. *Nature* **430**, 758–761 (2004).
3. K. J. Choi, M. Biegalski, Y. L. Li, A. Sharan, J. Schubert, R. Uecker, P. Reiche, Y. B. Chen, X. Q. Pan, V. Gopalan, L.-Q. Chen, D. G. Schlom, C. B. Eom, Enhancement of ferroelectricity in strained $BaTiO_3$ thin films. *Science* **306**, 1005–1009 (2004).
4. X. Moya, L. E. Hueso, F. Maccherozzi, A. I. Tovstolytkin, D. I. Podyalovskii, C. Ducati, L. C. Phillips, M. Ghidini, O. Hovorka, A. Berger, M. E. Vickers, E. Defay, S. S. Dhesi, N. D. Mathur, Giant and reversible extrinsic magnetocaloric effects in $La_{0.7}Ca_{0.3}MnO_3$ films due to strain. *Nat. Mater.* **12**, 52–58 (2013).
5. D. Sando, A. Agbelele, D. Rahmedov, J. Liu, P. Rovillain, C. Toulouse, I. C. Infante, A. P. Pyatakov, S. Fusil, E. Jacquet, C. Carrétéro, C. Deranlot, S. Lisenkov, D. Wang, J.-M. Le Breton, M. Cazayous, A. Sacuto, J. Juraszek, A. K. Zvezdin, L. Bellaiche, B. Dkhil, A. Barthélémy, M. Bibes, Crafting the magnonic and spintronic response of $BiFeO_3$ films by epitaxial strain. *Nat. Mater.* **12**, 641–646 (2013).
6. R. J. Zeches, M. D. Rossell, J. X. Zhang, A. J. Hatt, Q. He, C.-H. Yang, A. Kumar, C. H. Wang, A. Melville, C. Adamo, G. Sheng, Y.-H. Chu, J. F. Ihlefeld, R. Erni, C. Ederer, V. Gopalan, L.-Q. Chen, D. G. Schlom, N. A. Spaldin, L. W. Martin, R. Ramesh, A strain-driven morphotropic phase boundary in $BiFeO_3$. *Science* **326**, 977–980 (2009).
7. A. Vailionis, H. Boschker, W. Siemons, E. P. Houwman, D. H. A. Blank, G. Rijnders, G. Koster, Misfit strain accommodation in epitaxial ABO_3 perovskites: Lattice rotations and lattice modulations. *Phys. Rev. B* **83**, 064101 (2011).
8. H. S. Wang, Q. Li, Strain-induced large low-field magnetoresistance in $Pr_{0.67}Sr_{0.33}MnO_3$ ultrathin films. *Appl. Phys. Lett.* **73**, 2360–2362 (1998).
9. C. Adamo, X. Ke, H. Q. Wang, H. L. Xin, T. Heeg, M. E. Hawley, W. Zander, J. Schubert, P. Schiffer, D. A. Muller, L. Maritato, D. G. Schlom, Effect of biaxial strain on the electrical and magnetic properties of (001) $La_{0.7}Sr_{0.3}MnO_3$ thin films. *Appl. Phys. Lett.* **95**, 112504 (2009).
10. S. Valencia, L. Balcells, B. Martínez, J. Fontcuberta, Thickness dependence of the magnetic anisotropy in $La_{2/3}Ca_{1/3}MnO_3$ thin films grown on $LaAlO_3$ substrates. *J. Appl. Phys.* **93**, 8059–8061 (2003).
11. H. S. Wang, Q. Li, K. Liu, C. L. Chien, Low-field magnetoresistance anisotropy in ultrathin $Pr_{0.67}Sr_{0.33}MnO_3$ films grown on different substrates. *Appl. Phys. Lett.* **74**, 2212–2214 (1999).
12. J. L. MacManus-Driscoll, P. Zerrer, H. Wang, H. Yang, J. Yoon, A. Fouchet, R. Yu, M. G. Blamire, Q. X. Jia, Strain control and spontaneous phase ordering in vertical nanocomposite heteroepitaxial thin films. *Nat. Mater.* **7**, 314–320 (2008).
13. S. A. Harrington, J. Zhai, S. Denev, V. Gopalan, H. Wang, Z. Bi, S. A. T. Redfern, S.-H. Baek, C. W. Bark, C.-B. Eom, Q. X. Jia, M. E. Vickers, J. L. MacManus-Driscoll, Thick lead-free ferroelectric films with high Curie temperatures through nanocomposite-induced strain. *Nat. Nanotechnol.* **6**, 491–495 (2011).
14. J. MacManus-Driscoll, A. Suwardi, A. Kursumovic, Z. Bi, C.-F. Tsai, H. Wang, Q. X. Jia, O. J. Lee , New strain states and radical property tuning of metal oxides using a nanocomposite thin film approach. *APL Mater.* **3**, 062507 (2015).
15. Q. Zhan, R. Yu, S. P. Crane, H. Zheng, C. Kisielowski, R. Ramesh, Structure and interface chemistry of perovskite-spinel nanocomposite thin films. *Appl. Phys. Lett.* **89**, 172902 (2006).
16. X. Ning, Z. Wang, Z. Zhang, Large, temperature-tunable low-field magnetoresistance in $La_{0.7}Sr_{0.3}MnO_3$:NiO nanocomposite films modulated by microstructures. *Adv. Funct. Mater.* **24**, 5393–5401 (2014).
17. A. Chen, W. Zhang, F. Khatkatay, Q. Su, C.-F. Tsai, L. Chen, Q. X. Jia, J. L. MacManus-Driscoll, H. Wang, Magnetotransport properties of quasi-one-dimensionally channeled vertically aligned heteroepitaxial nanomazes. *Appl. Phys. Lett.* **102**, 093114 (2013).
18. N. M. Aimon, H. K. Choi, X. Y. Sun, D. H. Kim, C. A. Ross, Templated self-assembly of functional oxide nanocomposites. *Adv. Mater.* **26**, 3063–3067 (2014).
19. T. Fix, E.-M. Choi, J. W. A. Robinson, S. B. Lee, A. Chen, B. Prasad, H. Wang, M. G. Blamire, J. L. MacManus-Driscoll, Electric-field control of ferromagnetism in a nanocomposite via a ZnO phase. *Nano Lett.* **13**, 5886–5890 (2013).
20. W. Zhang, A. Chen, J. Jian, Y. Zhu, L. Chen, P. Lu, Q. X. Jia, J. L. MacManus-Driscoll, X. Zhang, H. Wang, Strong perpendicular exchange bias in epitaxial $La_{0.7}Sr_{0.3}MnO_3$:$BiFeO_3$ nanocomposite films through vertical interfacial coupling. *Nanoscale* **7**, 13808–13815 (2015).
21. H.-J. Liu, L.-Y. Chen, Q. He, C.-W. Liang, Y.-Z. Chen, Y.-S. Chien, Y.-H. Hsieh, S.-J. Lin, E. Arenholz, C.-W. Luo, Y.-L. Chueh, Y.-C. Chen, Y.-H. Chu, Epitaxial photostriction–magnetostriction coupled self-assembled nanostructures. *ACS Nano* **6**, 6952–6959 (2012).
22. C. Schmitz-Antoniak, D. Schmitz, P. Borisov, F. M. F. de Groot, S. Stienen, A. Warland, B. Krumme, R. Feyerherm, E. Dudzik, W. Kleemann, H. Wende, Electric in-plane polarization in multiferroic $CoFe_2O_4$/$BaTiO_3$ nanocomposite tuned by magnetic fields. *Nat. Commun.* **4**, 2051 (2013).
23. W. Zhang, A. Chen, Z. Bi, Q. X. Jia, J. L. MacManus-Driscoll, H. Wang, Interfacial coupling in heteroepitaxial vertically aligned nanocomposite thin films: From lateral to vertical control. *Curr. Opin. Solid State Mater. Sci.* **18**, 6–18 (2014).
24. S. Lee, A. Sangle, P. Lu, A. Chen, W. Zhang, J. S. Lee, H. Wang, Q. X. Jia, J. L. MacManus-Driscoll, Novel electroforming-free nanoscaffold memristor with very high uniformity, tunability, and density. *Adv. Mater.* **26**, 6284–6289 (2014).
25. Q. Su, D. Yoon, A. Chen, F. Khatkhatay, A. Manthiram, H. Wang, Vertically aligned nanocomposite electrolytes with superior out-of-plane ionic conductivity for solid oxide fuel cells. *J. Power Sources* **242**, 455–463 (2013).
26. Y.-H. Hsieh, J.-M. Liou, B.-C. Huang, C.-W. Liang, Q. He, Q. Zhan, Y.-P. Chiu, Y.-C. Chen, Y.-H. Chu, Local conduction at the $BiFeO_3$-$CoFe_2O_4$ tubular oxide interface. *Adv. Mater.* **24**, 4564–4568 (2012).
27. W. W. Li, W. Zhang, L. Wang, J. Gu, A. Chen, R. Zhao, Y. Liang, H. Guo, R. Tang, C. Wang, K. Jin, H. Wang, H. Yang, Vertical interface induced dielectric relaxation in nanocomposite $(BaTiO_3)_{1-x}$:$(Sm_2O_3)_x$ thin films. *Sci. Rep.* **5**, 11335 (2015).
28. V. Schuler, F. J. Bonilla, D. Demaille, A. Coati, A. Vlad, Y. Garreau, M. Sauvage-Simkin, A. Novikova, E. Fonda, S. Hidki, V. Etgens, F. Vidal, Y. Zheng, Huge metastable axial strain in ultrathin heteroepitaxial vertically aligned nanowires. *Nano Res.* **8**, 1964–1974 (2014).
29. J. L. MacManus-Driscoll, A. Suwardi, H. Wang, Composite epitaxial thin films: A new platform for tuning, probing, and exploiting mesoscale oxides. *MRS Bull.* **40**, 933–942 (2015).
30. A. Chen, Z. Bi, Q. X. Jia, J. L. MacManus-Driscoll, H. Wang, Microstructure, vertical strain control and tunable functionalities in self-assembled, vertically aligned nanocomposite thin films. *Acta Mater.* **61**, 2783–2792 (2013).
31. A. Chen, Z. Bi, C.-F. Tsai, J. Lee, Q. Su, X. Zhang, Q. X. Jia, J. L. MacManus-Driscoll, H. Wang, Tunable low-field magnetoresistance in $(La_{0.7}Sr_{0.3}MnO_3)_{0.5}$:$(ZnO)_{0.5}$ self-assembled vertically aligned nanocomposite thin films. *Adv. Funct. Mater.* **21**, 2423–2429 (2011).
32. A. Chen, M. Weigand, Z. Bi, W. Zhang, X. Lü, P. Dowden, J. L. MacManus-Driscoll, H. Wang, Q. X. Jia, Evolution of microstructure, strain and physical properties in oxide nanocomposite films. *Sci. Rep.* **4**, 5426 (2014).
33. V. Moshnyaga, B. Damaschke, O. Shapoval, A. Belenchuk, J. Faupel, O. I. Lebedev, J. Verbeeck, G. van Tendeloo, M. Mücksch, V. Tsurkan, R. Tidecks, K. Samwer, Structural phase transition at the percolation threshold in epitaxial $(La_{0.7}Ca_{0.3}MnO_3)_{1-x}$:$MgO_x$ nanocomposite films. *Nat. Mater.* **4**, 247–252 (2005).
34. W. Zhang, M. Fan, L. Li, A. Chen, Q. Su, Q. X. Jia, J. L. MacManus-Driscoll, H. Wang, Heterointerface design and strain tuning in epitaxial $BiFeO_3$:$CoFe_2O_4$ nanocomposite films. *Appl. Phys. Lett.* **107**, 212901 (2015).

35. H. Zheng, J. Kreisel, Y.-H. Chu, R. Ramesh, L. Salamanca-Riba, Heteroepitaxially enhanced magnetic anisotropy in $BaTiO_3$–$CoFe_2O_4$ nanostructures. *Appl. Phys. Lett.* **90**, 113113 (2007).
36. R. Zhao, W. W. Li, J. H. Lee, E. M. Choi, Y. Liang, W. Zhang, R. J. Tang, H. Y. Wang, Q. X. Jia, J. L. MacManus-Driscoll, H. Yang, Precise tuning of $(YBa_2Cu_3O_{7-\delta})_{1-x}$:$(BaZrO_3)_x$ thin film nanocomposite structures. *Adv. Funct. Mater.* **24**, 5240–5245 (2014).
37. A. Chen, W. Zhang, J. Jian, H. Wang, C.-F. Tsai, Q. Su, Q. X. Jia, J. L. MacManus-Driscoll, Role of boundaries on low-field magnetotransport properties of $La_{0.7}Sr_{0.3}MnO_3$-based nanocomposite thin films. *J. Mater. Res.* **28**, 1707–1714 (2013).
38. A. Chen, Z. Bi, H. Hazariwala, X. Zhang, Q. Su, L. Chen, Q. X. Jia, J. L. MacManus-Driscoll, H. Wang, Microstructure, magnetic, and low-field magnetotransport properties of self-assembled $(La_{0.7}Sr_{0.3}MnO_3)_{0.5}$:$(CeO_2)_{0.5}$ vertically aligned nanocomposite thin films. *Nanotechnology* **22**, 315712 (2011).
39. S. Lee, W. Zhang, F. Khatkhatay, Q. X. Jia, H. Wang, J. L. MacManus-Driscoll, Strain tuning and strong enhancement of ionic conductivity in $SrZrO_3$-RE_2O_3 (RE = Sm, Eu, Gd, Dy, and Er) nanocomposite films. *Adv. Funct. Mater.* **25**, 4328–4333 (2015).
40. J. Narayan, B. C. Larson, Domain epitaxy: A unified paradigm for thin film growth. *J. Appl. Phys.* **93**, 278–285 (2003).
41. Y. Zhu, P. Liu, R. Yu, Y.-H. Hsieh, D. Ke, Y.-H. Chu, Q. Zhan, Orientation-tuning in self-assembled heterostructures induced by a buffer layer. *Nanoscale* **6**, 5126–5131 (2014).
42. X. W. Wu, M. S. Rzchowski, H. S. Wang, Q. Li, Strain-induced magnetic properties of $Pr_{0.67}Sr_{0.33}MnO_3$ thin films. *Phys. Rev. B* **61**, 501–505 (2000).
43. J.-M. Hu, C. W. Nan, Electric-field-induced magnetic easy-axis reorientation in ferromagnetic/ferroelectric layered heterostructures. *Phys. Rev. B* **80**, 224416 (2009).
44. H. Zheng, J. Wang, L. Mohaddes-Ardabili, M. Wuttig, L. Salamanca-Riba, D. G. Schlom, R. Ramesh, Three-dimensional heteroepitaxy in self-assembled $BaTiO_3$–$CoFe_2O_4$ nanostructures. *Appl. Phys. Lett.* **85**, 2035–2037 (2004).
45. H. Pandey, P. K. Rout, Anupam, P. C. Joshi, Z. Hossain, R. C. Budhani, Magnetoelastic coupling induced magnetic anisotropy in $Co_2(Fe/Mn)Si$ thin films. *Appl. Phys. Lett.* **104**, 022402 (2014).
46. T. W. Darling, A. Migliori, E. G. Moshopoulou, S. A. Trugman, J. J. Neumeier, J. L. Sarrao, A. R. Bishop, J. D. Thompson, Measurement of the elastic tensor of a single crystal of $La_{0.83}Sr_{0.17}MnO_3$ and its response to magnetic fields. *Phys. Rev. B* **57**, 5093–5097 (1998).
47. R. V. Demin, L. I. Koroleva, A. M. Balbashov, Anomalies of magnetostriction and thermal expansion in $La_{0.7}Sr_{0.3}MnO_3$ perovskite. *J. Magn. Magn. Mater.* **177**, 871–872 (1998).
48. C. Cantoni, Y. Gao, S. H. Wee, E. D. Specht, J. Gazquez, J. Meng, S. J. Pennycook, A. Goyal, Strain-driven oxygen deficiency in self-assembled, nanostructured, composite oxide films. *ACS Nano* **5**, 4783–4789 (2011).
49. J. P. Perdew, M. Emzerhof, K. Burke, Rationale for mixing exact exchange with density functional approximations. *J. Chem. Phys.* **105**, 9982–9985 (1996).
50. P. C. Dowden, Z. Bi, Q. X. Jia, Method for controlling energy density for reliable pulsed laser deposition of thin films. *Rev. Sci. Instrum.* **85**, 025111 (2014).
51. L.-Q. Chen, Phase-field models for microstructure evolution. *Annu. Rev. Mater. Res.* **32**, 113–140 (2002).
52. J.-M. Hu, T. Yang, J. Wang, H. Huang, J. Zhang, L.-Q. Chen, C.-W. Nan, Purely electric-field-driven perpendicular magnetization reversal. *Nano Lett.* **15**, 616–622 (2015).
53. J. J. Wang, X. Q. Ma, Q. Li, J. Britson, L.-Q. Chen, Phase transitions and domain structures of ferroelectric nanoparticles: Phase field model incorporating strong elastic and dielectric inhomogeneity. *Acta Mater.* **61**, 7591–7603 (2013).
54. D. Sander, The correlation between mechanical stress and magnetic anisotropy in ultrathin films. *Rep. Prog. Phys.* **62**, 809–858 (1999).
55. R. O. Bell, G. Rupprecht, Elastic constants of strontium titanate. *Phys. Rev.* **129**, 90–94 (1963).
56. G. Carlotti, G. Socino, A. Petri, E. Verona, Acoustic investigation of the elastic properties of ZnO films. *Appl. Phys. Lett.* **51**, 1889–1891 (1987).
57. Q. Y. Qiu, V. Nagarajan, S. P. Alpay, Film thickness versus misfit strain phase diagrams for epitaxial $PbTiO_3$ ultrathin ferroelectric films. *Phys. Rev. B* **78**, 064117 (2008).
58. R. People, J. C. Bean, Calculation of critical layer thickness versus lattice mismatch for Ge_xSi_{1-x}/Si strained-layer heterostructures. *Appl. Phys. Lett.* **47**, 322–324 (1985).
59. J. L. Vassent, M. Dynna, A. Marty, B. Gilles, G. Patrat, A study of growth and the relaxation of elastic strain in MgO on Fe(001). *J. Appl. Phys.* **80**, 5727–5735 (1996).
60. L. W. Martin, Y.-H. Chu, R. Ramesh, Advances in the growth and characterization of magnetic, ferroelectric, and multiferroic oxide thin films. *Mater. Sci. Eng. R* **68**, 89–133 (2010).

Acknowledgments
Funding: This work was supported by the U.S. Department of Energy (DOE) through the National Nuclear Security Administration's (NNSA's) Laboratory Directed Research and Development Program and performed, in part, at the Center for Integrated Nanotechnologies, an Office of Science User Facility operated for the U.S. DOE Office of Science. Los Alamos National Laboratory (LANL), an affirmative action equal opportunity employer, is operated by Los Alamos National Security, LLC, for the NNSA of the U.S. DOE under contract DE-AC52-06NA25396. The work at Pennsylvania State University is supported by U.S. National Science Foundation (NSF) (grant nos. DMR-1410714 to T.Y. and L.-Q.C and DMR-1235092 to J.-M.H. and L.-Q.C.) and partially by the Hamer Professorship of Materials Science and Engineering (J.-M.H. and L.-Q.C.). Sandia National Laboratories is a multiprogram laboratory managed and operated by Sandia Corporation, a wholly owned subsidiary of Lockheed Martin Corporation, for the U.S. DOE's NNSA under contract DE-AC04-94AL85000. J.L.M.-D. thanks the European Research Council (ERC) for the Advanced Investigator Grant, Novox, ERC-2009-adG 247276. The effort at Texas A&M University is supported by the U.S. NSF (DMR-0846504 and 141266). A.C. thanks LANL Postdoctoral Program for Director's Postdoctoral Fellowship. **Author contributions:** A.C., E.E., and Q.X.J. designed and coordinated the experiments, grew samples, and performed XRD. M.W. and A.C. performed the magnetotransport and magnetization measurements. P.L., A.C., W.Z., L.L., and H.W. characterized the microstructure. J.-M.H., T.Y., and L.-Q.C. performed the phase-field simulations. T.A. and J.-X.Z. performed the DFT calculations. All authors discussed the results and commented on the manuscript. **Competing interests:** The authors declare that they have no competing interests. **Data and materials availability:** All data needed to evaluate the conclusions in the paper are present in the paper and/or the Supplementary Materials. Additional data related to this paper may be requested from the authors. Please direct all inquiries to the corresponding authors.

Submitted 5 February 2016
Accepted 19 May 2016
Published 10 June 2016
10.1126/sciadv.1600245

Citation: A. Chen, J.-M. Hu, P. Lu, T. Yang, W. Zhang, L. Li, T. Ahmed, E. Enriquez, M. Weigand, Q. Su, H. Wang, J.-X. Zhu, J. L. MacManus-Driscoll, L.-Q. Chen, D. Yarotski, Q. X. Jia, Role of scaffold network in controlling strain and functionalities of nanocomposite films. *Sci. Adv.* **2**, e1600245 (2016).